Protein nanopore reveals the renin–angiotensin system crosstalk with single-amino-acid resolution

Jie Jiang[1,4], Meng-Yin Li[1,2,4], Xue-Yuan Wu[1], Yi-Lun Ying [1,2], Huan-Xing Han[3] & Yi-Tao Long [1]✉

The discovery of crosstalk effects on the renin–angiotensin system (RAS) is limited by the lack of approaches to quantitatively monitor, in real time, multiple components with subtle differences and short half-lives. Here we report a nanopore framework to quantitatively determine the effect of the hidden crosstalk between angiotensin-converting enzyme (ACE) and angiotensin-converting enzyme 2 (ACE2) on RAS. By developing an engineered aerolysin nanopore capable of single-amino-acid resolution, we show that the ACE can be selectively inhibited by ACE2 to prevent cleavage of angiotensin I, even when the concentration of ACE is more than 30-fold higher than that of ACE2. We also show that the activity of ACE2 for cleaving angiotensin peptides is clearly suppressed by the spike protein of SARS-CoV-2. This leads to the relaxation of ACE and the increased probability of accumulation of the principal effector angiotensin II. The spike protein of the SARS-CoV-2 Delta variant is demonstrated to have a much greater impact on the crosstalk than the wild type.

The renin–angiotensin system (RAS) acts as a critical guard that protects the human body from a loss of blood pressure or an electrolyte imbalance[1,2]. Dysregulation of this system causes cardiovascular disease, which is the leading cause of death worldwide[3,4]. Traditional clinical therapies for pathological RAS activation focus mainly on the principal effector peptide angiotensin II (Ang II), involving inhibitors of its formation enzyme ACE (angiotensin-converting enzyme) or treatment with Ang II receptor antagonists[5]. In fact, endogenous ACE2, another angiotensin-converting enzyme, could also reduce Ang II levels and degrade its precursor Ang I into Ang 1–9 (Fig. 1b). Moreover, emerging evidence has demonstrated that Ang 1–7, cleaved from Ang II by ACE2, exhibits entirely opposite actions towards Ang II, suggesting the counter-regulatory role of ACE2 in the activation of the RAS[6,7]. Therefore, the crosstalk effect of ACE2 and ACE indeed has complex effects on the RAS[1,2], and thus might provide novel in-depth insights into the RAS regulation mechanism. The individual catalytic features

of ACE and ACE2 are well established[8], but the crosstalk effect between them remains undetermined[2,6]. Moreover, recently, the COVID-19 pandemic has directed scientists' attention back to ACE2, as it is the leading receptor reported on human cells to be bound by the spike protein (SP) of SARS-CoV-2[9,10]. To our knowledge, when the cells are attacked by the coronavirus, the crosstalk of ACE and ACE2 is further perturbed, leading to the characteristic symptoms[11].

Studies of the enzyme crosstalk effect rely on the simultaneous real-time discrimination of substrates with subtle structural differences, given the short half-life of the subsequent enzyme reaction[1]. However, the current fluorescence-based method depends heavily on complex multicoloured label design[12,13], and mass spectrometry (MS) shows limited ability to provide dynamic information[14,15]. Moreover, the quantification of each substrate presents the additional challenge to avoid obtaining the average characteristics from ensemble measures. The nanopore has been developed as a powerful high-throughput

[1]State Key Laboratory of Analytical Chemistry for Life Science, School of Chemistry and Chemical Engineering, Nanjing University, Nanjing, China. [2]Chemistry and Biomedicine Innovation Center, Nanjing University, Nanjing, China. [3]Department of Pharmacy, Shanghai Changzheng Hospital, Shanghai, China. [4]These authors contributed equally: Jie Jiang, Meng-Yin Li. ✉e-mail: yitaolong@nju.edu.cn
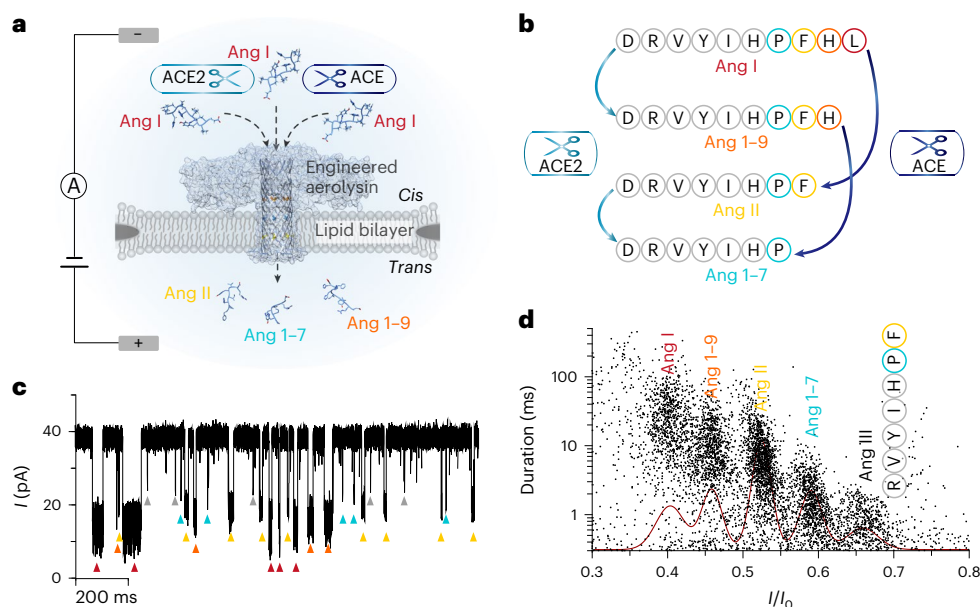
Fig. 1 | Discrimination of Ang peptide substrates for ACE and ACE2 with the engineered aerolysin nanopore. a, Illustration of the aerolysin-based nanopore framework for detecting Ang peptides cleaved by ACE and/or ACE2. **b**, Metabolism pathways of Ang I regulated by ACE and ACE2. Ang peptides, including Ang I, Ang 1–9, Ang II and Ang 1–7, differ in only one C-terminal amino acid. **c,d**, Raw current traces (**c**) and the corresponding scatter plots (**d**) of the mixture of Ang I, Ang 1–9, Ang II, Ang 1–7 and Ang III observed in the T232K engineered aerolysin platform. The red curve represents the Gaussian fitting to the I/I_0 histogram of the mixture (I and I_0 represent residual current and open pore current, respectively), in which the data were acquired in 1.0 M KCl with 10 mM Tris and 1.0 mM EDTA at pH 8.0 under an applied potential of +140 mV. The current was sampled at 100 kHz and filtered at 5 kHz. The colours used for the Ang peptides are consistent in all panels.

single-molecule method to determine the features of a single molecule, in terms of its size[16–18], charge[19–21] and conformation[22–24], for example. Given that only one molecule at a time can enter the nanopore to induce the characteristic current event, the nanopore approach could be used to identify the properties of each individual molecule without losing the information for low-abundance molecules. More importantly, in contrast to other single-molecule approaches such as single-molecule force spectroscopy, which examines each molecule for a long time, continuous reading of different individual molecules over short intervals[25,26] enables the nanopore approach to monitor the dynamic transformation processes of a series of biomolecules in a complex system.

In this Article we first describe the establishment of a nanopore framework to reveal crosstalk effects in the RAS, based on the following three criteria: (1) sufficient resolution to identify peptides with one-amino-acid difference; (2) high capture efficiency to ensure real-time analysis; (3) proper conditions for peptide detection that are compatible with the enzyme reaction environment. These features allow us to utilize the engineered aerolysin platform to achieve real-time monitoring of the evolution of multiple substrates and also quantify instantaneous intermediates in a mixed enzyme reaction system. The results reflect an amazing inhibition of ACE by ACE2 for cleaving Ang I with a concentration ratio of ACE and ACE2 of 1:0.64 and 1:0.16, but almost no influence on ACE activity for degrading Ang 1–9. The intermediate Ang II was not generated until the concentration ratio of ACE:ACE2 decreased to about 1:0.03. Furthermore, the effect of the SARS-CoV-2 SP on this system was illustrated, demonstrating the infection of ACE2 by the SARS-CoV-2 SP with an efficiency quantified as 2.96 ± 0.58 U mg^{-1}, leading to increased ACE-mediated Ang peptide production. More interestingly, the SP of the SARS-CoV-2 Delta variant further induced a great enhancement to about threefold production and fourfold accumulation of Ang II compared to the wild-type (WT) SP, suggesting that the inhibition of ACE activity for Ang I cleavage by ACE2 has almost disappeared.

Results and discussions

Reading Ang peptides at single-amino-acid resolution with high accuracy and efficiency

Aerolysin has a unique geometric structure, with a narrow (~1.0 nm) and long (~10 nm) channel and without a vestibule, that provides a superconfined environment for single-molecule sensing. This confined space leads to high sensitivity for the detection, identification and discrimination of highly charged DNA or homopolypeptides, even those with only one nucleobase or amino-acid difference from WT aerolysin[18,20,26–29]. An engineered FraC nanopore has been used previously to identify Ang peptides[30,31]. However, accurate discrimination of Ang peptides differing by a single amino acid in a mixture is crucial for unveiling the crosstalk between ACE and ACE2. Given the ultralow charges carried by Ang peptides (Supplementary Table 1), which is one of the challenges for nanopore-based peptide sensing, the aerolysin was further engineered to introduce electroosmotic flow and enhance the interactions with target peptides (Fig. 1a). Among the engineered aerolysin candidates with different mutations, the T232K aerolysin nanopore exhibited the longest duration and highest capture efficiency for the model molecule Ang I (Supplementary Figs. 1 and 2). These results can be ascribed to the enhancement of electroosmotic flow by the positive charges of lysine, the narrow radius and the longer side chain of lysine, and the introduction of an extra potential fluctuation region inside the T232K mutant aerolysin (Supplementary Figs. 3 and 4). In addition, to balance the detection stability and high duration/capture efficiency, the applied voltage was fixed to +140 mV in the following nanopore experiments, based on the voltage-dependent duration and frequency of Ang I in T232K aerolysin (Supplementary Fig. 5). Because the long duration ensures sufficient current resolution, T232K could identify all five Ang peptides in the mixture—Ang I, Ang 1–9, Ang II, Ang 1–7 and Ang III (which differ in only one amino acid)—by direct readout of these peptides as clearly distinguishable residual current populations (Fig. 1b–d). Considering the characteristic current fluctuations for each Ang peptide inside the nanopore (Supplementary

Fig. 6a), the resolution of T232K aerolysin for distinguishing the Ang peptides could be further improved by combining it with the residual current standard deviation (s.d.) of each blockage (Supplementary Fig. 6b,c). It should be noted that the assignment of five residual currents was further determined by the successive addition of the Ang peptide samples to the detection system (Supplementary Fig. 7).

Construction of the nanopore framework for Ang I cleavage recording

With a view to determining the peptide cleavage activities of ACE and ACE2, the constructed T232K nanopore platform was then evaluated for its single-molecule detection of Ang peptides while in the enzyme functional environment. To balance the activity of ACE/ACE2 and the signal-to-noise ratio of the current recording, the salt concentration was set to 1.0 M KCl with 10 mM HEPES and 10 μM $ZnCl_2$ at pH 8.0, defined as HEPES-KCl buffer, because ACE and ACE2 are zinc metalloproteases[11]. It was noted that the ACE and ACE2 catalytic activities are enhanced by the monovalent anion of Cl^-, thus ensuring the intrinsic adaptability of the nanopore for the reaction study[32]. As shown in Supplementary Fig. 8, the T232K aerolysin detection system is stable in the HEPES-KCl environment, with virtually no background signal. More importantly, the five Ang peptides (Ang I, Ang 1–9, Ang II, Ang 1–7 and Ang III) can also be explicitly identified and distinguished from one another in this environment, as shown in Supplementary Fig. 9. This observation shows that the constructed T232K aerolysin framework clearly meets the three critical criteria described above, thus enabling us to reveal the crosstalk effects in the RAS.

To further verify the biological activities of ACE and ACE2 in the detection system, we examined the hydrolysis of Ang I by ACE or ACE2. As shown in Fig. 2a, sequential loss of the characteristic blockade corresponding to Ang I was observed, along with the concurrent appearance of blockades with increased residual current ratio I/I_0 and shorter duration. In terms of the current population of the mixed sample, the new blockades were generated by the addition of Ang II, demonstrating hydrolysis of Ang I by ACE (Supplementary Fig. 10). Moreover, only two blockades, referred to as Ang I and Ang II, were detected throughout the entire hydrolysis process, indicating that Ang II was the sole decomposition product derived from Ang I by ACE alone. Based on the continuous current recording, the complete evolution process for Ang I and Ang II during the entire enzymatic reaction could be observed by analyzing means of I/I_0 and the absolute time when the events occurred (Fig. 2b). As shown in Fig. 2c, by combining the capture efficiency of Ang I and Ang II in T232K aerolysin as presented in Supplementary Fig. 11, the concentrations of Ang I and Ang II were calculated every minute, demonstrating the real-time nature of the nanopore approach (details are provided in the Methods, Supplementary Figs. 12–14 and Supplementary Table 2). Moreover, based on the substrate concentration-dependent catalytic velocity, the kinetic constants (k_{cat} and k_M) of ACE could be calculated by using the Michaelis–Menten equation. Here, k_{cat} and k_M represent the Michaelis constant and turnover number, respectively. As shown in Fig. 2d, according to the Lineweaver–Burk plot, the k_{cat} and k_M of ACE for Ang I (10.8 ± 1.1 min^{-1} and 12.8 ± 0.9 μM, respectively) in the nanopore measurements are comparable but obviously lower than those found in previous studies (approximately 660 min^{-1} and 70 μM for Ang I in 0.3 M NaCl at pH 7.5)[33]. This could be ascribed to chloride inhibition at over-high concentrations, especially at concentrations higher than 800 mM (ref. [34]).

Similarly, the gradual appearance of the characteristic blockades for Ang 1–9 was also observed during hydrolysis by ACE2, as shown in Fig. 2e and Supplementary Fig. 15. Ang 1–9 is the only product of Ang I produced by ACE2. As presented in Fig. 2f–h, ACE2 exhibited a greater hydrolysis efficiency for Ang I than ACE under the experimental conditions (calculated k_{cat} and k_M of ~64.8 $\pm$ 5.1 min^{-1} and 20.2 $\pm$ 1.1 μM, respectively). Notably, the standard errors of the kinetic constants arose from the three independent measurements. More interestingly, an abnormal Lineweaver–Burk plot was observed for ACE2 with a low concentration of Ang I (Fig. 2h, blue area), which suggests a complicated mechanism for the reaction with low occupancy of the substrate Ang I and high occupancy of the product Ang 1–9. This observation, as well as the kinetic features of ACE and ACE2 measured above, were also confirmed by MS, as shown in Supplementary Figs. 16–19. To further validate the catalysis efficiency of the enzymes measured in the nanopore approach, the hydrolysation by ACE2 of human β-casomorphin (Cas-7) and neurotensin 1–8 (Neu 1–8) was monitored using T232K mutant aerolysin (details are provided in the Methods). As shown in Supplementary Figs. 20–23, by distinguishing Cas-7 from its product Cas-6, and Neu 1–8 from Neu 1–7, ACE2 showed obviously larger conversion rates (k_{cat}) for Cas-6 (~115.6 $\pm$ 4.9 min^{-1}) and Neu 1–8 (~1,312.2 $\pm$ 29.7 min^{-1}), and a much greater k_M value for Neu 1–8 (181.2 $\pm$ 2.6 μM) than for Ang I, which is quite consistent with the previous results regarding the efficiency of ACE2 for Ang I, Cas-7 and Neu 1–8[32].

Crosstalk between ACE and ACE2

To explore the crosstalk effects between ACE and ACE2 in the RAS, we further profiled the peptide substrate transformation in the presence of both ACE and ACE2. As shown in Fig. 3a (left panel) and Supplementary Fig. 7, immediately following the addition of the ACE and ACE2 enzyme mixture (36 nM ACE and 23 nM ACE2) to the peptide substrate Ang I, the amount of Ang I decreased significantly, while the populations corresponding to the other three Ang peptides increased successively. Towards the end, after more than 4 h, all the peptides were transformed almost completely to just one species (Fig. 3a and Supplementary Fig. 24). According to the residual currents of the Ang peptide mixture, the first two population increases were attributed to Ang 1–9 and Ang 1–7, and the final population was demonstrated to be induced by the Ang 1–5 by adding the peptide to the final digestion solution (Supplementary Fig. 25). Surprisingly, Ang II, which was expected to be generated by ACE cleavage of Ang I, was not observed at all during the entire catalysis process. To clarify why Ang II did not appear during the reaction, we calculated the concentrations of Ang peptides every 1 min (details are provided in the Supplementary Methods). As shown in the left panel of Fig. 3c, the stepwise conversion from Ang I to Ang 1–9, Ang 1–7 and Ang 1–5 clearly demonstrates the absence of Ang II. More importantly, the conversion velocity of Ang I was almost the same as that during the reaction in which ACE2 cleaved Ang I alone, as shown in Fig. 2f,g, demonstrating that the absence of Ang II was not caused by immediate degradation by ACE2. Considering that the production of Ang 1–7 and Ang 1–5 indeed requires the assistance of ACE, these results suggest that the activity of ACE is severely and selectively suppressed by ACE2, which acts only on the production of Ang II (Fig. 3d, left).

To further confirm and study the selective inhibition of ACE by ACE2 for only Ang I cleavage, experiments at a lower salt concentration (0.50 M KCl) were performed to examine the potential chloride inhibition of ACE at over-high concentrations, as mentioned above[34]. As illustrated in Supplementary Figs. 26–28, Ang II was still not observed during the reaction, and the conversion of Ang I slowed, which could be attributed to the weakened activity of ACE2 at the low Cl^- concentration. These observations support that the absence of Ang II is not caused by immediate degradation by ACE2, and further suggest that the inhibition of ACE by ACE2 is not simply caused by competition with the substrate. Furthermore, even at the physiologically relevant salt concentration (0.15 M), although the activity of ACE2 for Ang I was greatly weakened, as described in previous work[32], selective inhibition of ACE by ACE2 for only Ang I cleavage was still observed, with barely any current events recorded for Ang II (Supplementary Figs. 29 and 30), indicating that this crosstalk between them was stable at chloride concentrations ranging from 0.15 M to 1.0 M. This is thus a clear observation of the enzyme crosstalk effect in the RAS. Notably, the crosstalk between ACE and ACE2 in 1.0 M and 0.15 M KCl was confirmed by using
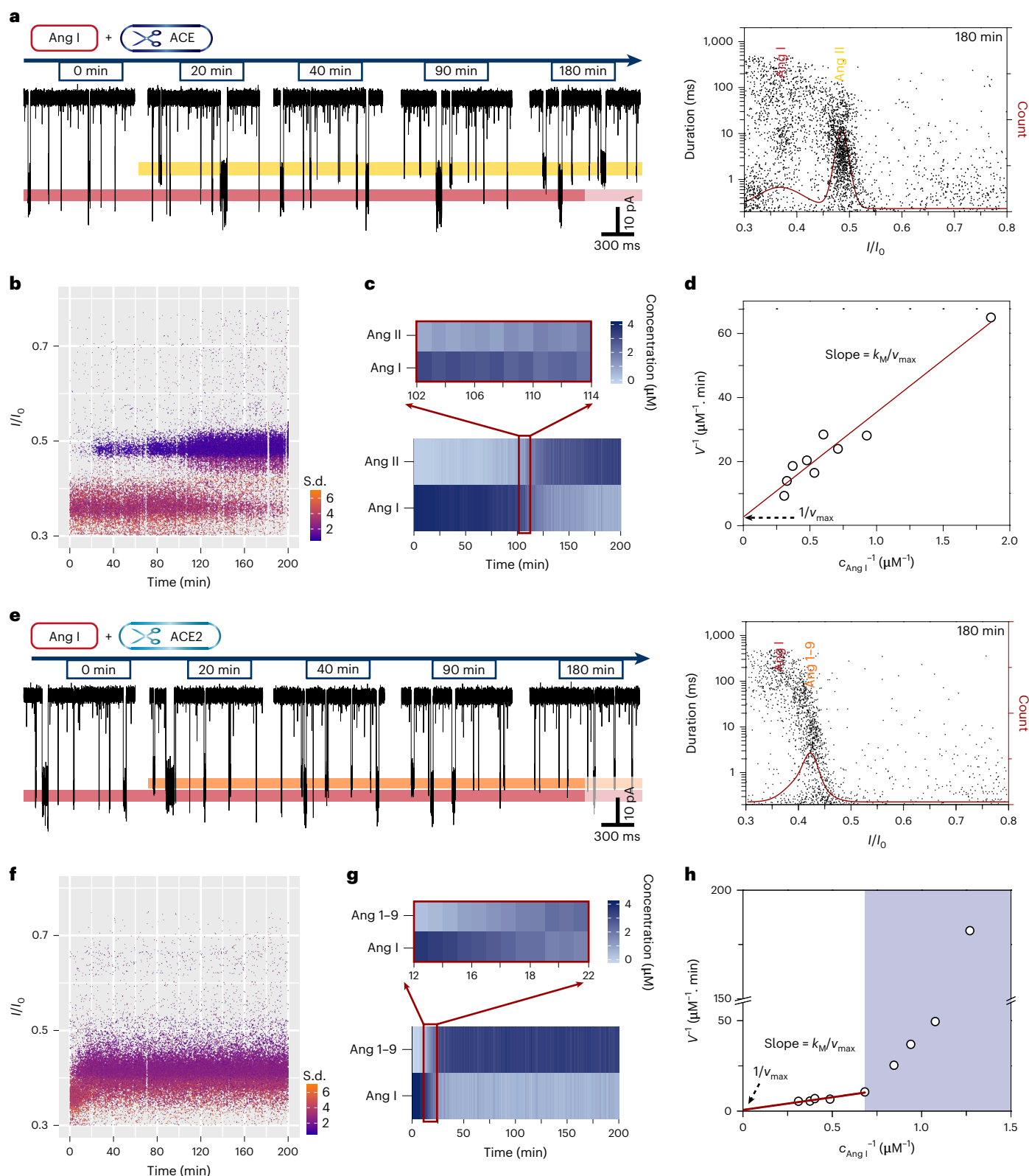
Fig. 2 | Recording the evolution of Ang I mediated by ACE or ACE2. a, Left: raw current traces for Ang I cleaved by ACE at 0, 20, 40, 90 and 180 min. Right: scatter plots (black dots) and Gaussian fitting (red line) for the corresponding I/I_0 histogram of Ang I cleaved by ACE after 180 min. **b,c**, I/I_0 of the events versus reaction time (**b**) and evolution of Ang I and Ang II (**c**) during ACE cleavage of Ang I. The colours in **b** and **c** represent the s.d. of each current event and the concentration of Ang peptides, respectively. **d**, Lineweaver–Burk plot of ACE cleaving Ang I. Here, V and v_{max} represent the reaction velocity and the maximum reaction velocity, respectively, and c is the concentration of the peptide. **e**, Left: raw current traces of Ang I cleaved by ACE2 at 0, 20, 40, 90 and 180 min. Right: scatter plots (black dots) and Gaussian fitting (red line) for the corresponding I/I_0 histogram of Ang I cleaved by ACE2 after 180 min. **f,g**, I/I_0 of the events versus reaction time (**f**) and evolution of Ang I and Ang 1–9 (**g**) during ACE2 cleavage of Ang I. **h**, Lineweaver–Burk plot of ACE2 cleaving Ang I. The data were acquired in 1.0 M KCl with 10 mM HEPES and 10 μM $ZnCl_2$ at pH 8.0 under an applied potential of +140 mV. The concentrations of ACE and ACE2 were 36 nM and 23 nM, respectively, with 4.0 μM Ang I substrate, and the reaction temperature was set to 21 ± 1 °C. The current was sampled at 100 kHz and filtered at 5 kHz.
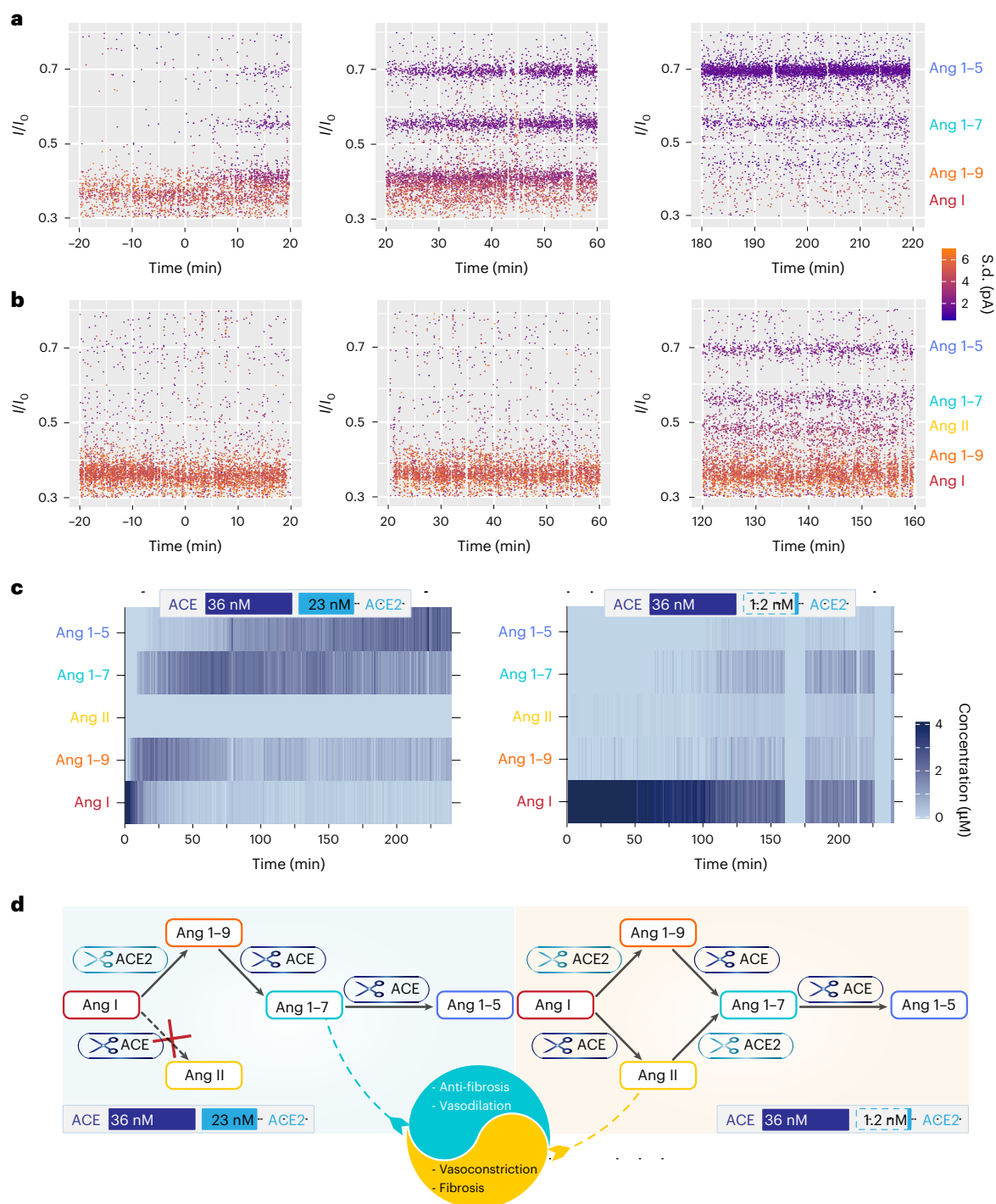
Fig. 3 | Real-time monitoring of the enzymatic degradation of Ang I by ACE2 and ACE. a,b, I/I_0 of the events versus reaction time while Ang I is cleaved by the enzyme mixture (36 nM ACE and 23 nM ACE2 for **a**; 36 nM ACE and 1.2 nM ACE2 for **b**). **c**, Evolution of Ang I, Ang 1–9, Ang II, Ang 1–7 and Ang 1–5 during the reaction of Ang I cleaved by the ACE and ACE2 mixture with different concentration ratios. The concentrations were calculated every 1 min. The colour represents the concentration of each Ang peptide. **d**, Illustration of the transition route for Ang I degradation by ACE and ACE2 with concentrations of 36 nM and 23 nM, respectively (left), and 36 nM and 1.2 nM, respectively (right). The data were acquired in 1.0 M KCl with 10 mM HEPES and 10 µM ZnCl₂ at pH 8.0, under an applied potential of +140 mV. The initial concentration of substrate Ang I was 4.0 µM, and the reaction temperature was set to 21 ± 1 °C. The current was sampled at 100 kHz and filtered at 5 kHz.

traditional MS (Supplementary Figs. 31 and 32). Given the catalytic mechanism and behaviour of ACE reported previously, the two active domains of ACE (N domain and C domain) have obvious differences in terms of substrate specificity and chloride ion dependence[35]. Although the N domain of ACE exhibited a high hydrolysis efficiency of Ang 1–7

with low Cl⁻ dependence[36], its C domain dominated the cleavage of Ang I among all the ACE[37], almost without activity for Ang 1–7, and was highly activated by Cl⁻. Therefore, the crosstalk between ACE and ACE2 may be mainly attributable to the effects of ACE2 on the C domain of ACE, such as ACE2 transient interaction/binding with the ACE C domain

and/or hydrolysis of several terminal amino acids, leading to a change in C-domain activity for Ang I cleavage.

We also explored the effect of the concentration ratio of ACE2 and ACE on the production of Ang II in this crosstalk system. The results showed that a decrease in ACE2 concentration to 5.8 nM with ACE kept constant had almost no effect in comparison with the catalytic tendency of ACE2 at 23 nM, as described above (Supplementary Fig. 33), but the gradually producing of Ang II was observed when the ACE2 concentration was decreased to 1.2 nM (~30-fold lower than ACE), as shown in Fig. 3b. However, the observation of Ang 1–9 indicated that ACE2 was active, even when present at such a low enzyme proportion, suggesting that both the ACE pathway and the ACE2 pathway function in the same process of Ang I degradation, as illustrated in Fig. 3d. Longer monitoring of the catalytic processes was performed to ensure the stability of ACE2 with such low activity (Supplementary Fig. 34). Moreover, from a comparison of the Ang II frequency–time curve induced by the ACE enzyme alone (Fig. 2b,c), we observed that the release of Ang II was reduced during the same time period, reflecting the inhibitory effects of ACE2 in the ACE pathway on Ang II formation. More interestingly, increasing the initial substrate, Ang I, did not change the catalysis tendency (Supplementary Fig. 35), and ACE and ACE2 could simultaneously hydrolyse Ang I and Ang 1–9, Ang I and Ang II, respectively, in their mixture (Supplementary Figs. 36 and 37), further supporting the complex inhibition of ACE by ACE2 rather than competition for the substrate. These results further demonstrate the extensive and selective inhibition of ACE by ACE2 and provide a critical regulatory ratio for weakening or even preventing the production of Ang II. Traditionally, the downregulation of Ang II accumulation in vivo is achieved mainly by the use of ACE inhibitors. However, the inhibition of ACE activity could also greatly affect the balance of Ang 1–7 in human systems (including production and metabolism), while Ang 1–7 has extra functions beyond inhibiting the function of Ang II[1,6]. As illustrated in Fig. 3c, the crosstalk between ACE and ACE2 suggests that ACE2 could potentially be regarded as a regulatory target, the slight upregulation of which could effectively reduce Ang II production while maintaining the balance of Ang 1–9 and Ang 1–7.

Influence of the SARS-CoV-2 spike protein

As ACE2 has been regarded as the cellular receptor of SARS-CoV-2, we employed the present approach to gain deeper insights into the pathogenic pathway of this global health risk, and attempted to optimize treatment for infected patients[11]. Because the spike protein (SP) of SARS-CoV-2 binds to the N-terminal region of ACE2 to infect mammalian cells, as illustrated in Fig. 4a[9,10], the SP was used to evaluate the effects of SARS-CoV-2 in this crosstalk system. After 30 min of incubation at 20 °C, the mixture of SP, ACE and ACE2 (concentration ratio of ACE and ACE2 of 1:0.03) was added to a detection system that contained Ang I (details are provided in the Supplementary Information). As shown in Fig. 4b and Supplementary Fig. 38, SP obviously reduced the production of Ang 1–9, Ang 1–7 and Ang 1–5, while, surprisingly, the proportion of Ang II increased. These observations indicate that the existence of SP could consume ACE2, leading to a decrease in ACE2-based cleavage of Ang peptides. Because the conversion of Ang I to Ang 1–9, Ang 1–7 or Ang 1–5 is mediated by ACE2 only once, as illustrated in Fig. 4c, inhibition of ACE2 by the SP of SARS-CoV-2 could be estimated. As shown in Fig. 4d, the inhibition by SP of the ACE2-based cleavage quantity was, surprisingly, proportional to the reaction time, with an inhibition efficiency of -2.96 ± 0.58 U (ACE2) mg^{-1} (SP) (details are provided in the Methods; the s.d. was derived from estimations at four time points). More interestingly, the occupancy of Ang II increased at each time point, demonstrating the higher ACE activity for Ang I cleavage in the presence of SP, which further suggested a decrease in the inhibition of ACE by ACE2. However, the change in ACE-based cleavage quantity by SP exhibited a non-monotonic correlation with reaction time (Fig. 4e), which might be ascribed to counteraction of the weakened

ACE2 activity by the enhanced ACE activity for producing Ang 1–7 and Ang 1–5. It should be noted that, with inhibition of ACE2 by SP further confirmed by MS, and in a physiological salt concentration (Supplementary Figs. 39 and 40), the effect of the SP of SARS-CoV-2 on the activity of ACE2 in our experiments seems to be opposite to those reported previously[38–40]. This could be explained in two ways. First, considering that the determination of ACE2 activity in these works is based mainly on the cleavage of Mca-YVADAPK-Dnp[38,39,41], the different influences of SP on ACE2 activity might be caused by the different substrates, because the small lobe contacted by the SP forms the peptide substrate-binding site of ACE2 with another lobe[9]. Furthermore, the fluorophores used to label the substrate could introduce an extra effect on the interactions between the substrate and ACE2, which might further lead to a change in the effect of SP on ACE2 activity. In principle, the nanopore approach without labelling could show the 'intrinsic' interplay between proteins, which should be close to that occurring in vivo. Moreover, the relatively constant Ang 1–5/Ang II levels, with their lower absolute concentrations in patients with COVID-19[40], indeed reflect the lower activity for each ACE2 molecule, and the downregulation of ACE2 with a concomitant increase in Ang II in the lung tissue or vascular endothelial cells by the isolated SP[42,43] is also consistent with the results obtained in nanopore measurements. Second, given that ACE2 could selectively inhibit the activity of ACE for Ang I cleavage, to study the potential effect of ACE on ACE2 activity in the presence of SP, the influences of SP on ACE2 without ACE were tested. As shown in Supplementary Fig. 41, without ACE, the change in ACE2-based cleavage quantity decreased under SP induction, indicating the potential effect of ACE on the inhibition of ACE2 by SP. In addition, the excessive SP used in nanopore experiments and the ACE2-concentration-dependent SP inhibition efficiency suggest a complicated mechanism of action between them (Supplementary Fig. 42).

Furthermore, as the Delta variant of SARS-CoV-2 is highly contagious and had accounted for the most COVID-19 cases in the world, the effects of the SP of the Delta variant on the crosstalk between ACE and ACE2 were evaluated. Because the Delta variant shows higher binding affinity with ACE2 and has several mutations in the receptor-binding domain (RBD), including L452R and T478K in the receptor-binding motif (RBM) (Fig. 4f), the binding between ACE2 and the SP of the Delta variant (called Delta SP) might exhibit some changes compared to the WT SP. To our surprise, Ang II became the leading product at each time point in the presence of the Delta SP (Fig. 4g), which was never observed during the reaction in the presence of the WT SP or without the SP, demonstrating an obvious enhancement of both Ang II production and accumulation (Fig. 4h). These results further demonstrated the disappearance of inhibition of ACE2 to ACE for Ang I cleavage in this system. Given that the over-accumulation of Ang II would not only disturb the RAS, but also affect the central nervous system and even the immune system[2,6], the observation of the higher level of Ang II induced by the Delta SP might be related to the severe illness and potential cytokine storm observed in some patients with COVID-19 infected with the Delta variant.

In summary, we have reported a nanopore framework to intrinsically screen the crosstalk effects between ACE2 and ACE in a complex environment. By directly reading a number of individual molecules of multiple Ang peptides during the enzymic process, not only was the selective inhibition of ACE by ACE2 clearly illustrated, but also the influences of the SARS-CoV-2 SP. The results demonstrate that the binding of the SARS-CoV-2 SP and ACE2 could weaken the crosstalk effect of ACE and ACE2, leading to accumulation of vasoconstriction and the fibrosis factor Ang II. This suppression of ACE2 by SARS-CoV-2 demonstrates another explicit advantage of the nanopore framework, which could overcome the inevitable perturbation of the enzymatic process induced by extra modifications involved in other single-molecule methods, such as fluorescence-based approaches. More interestingly, with the concentration of the SP remaining much higher than that of ACE2 based on binding affinity, promotion of this suppression of ACE2 by the SP was
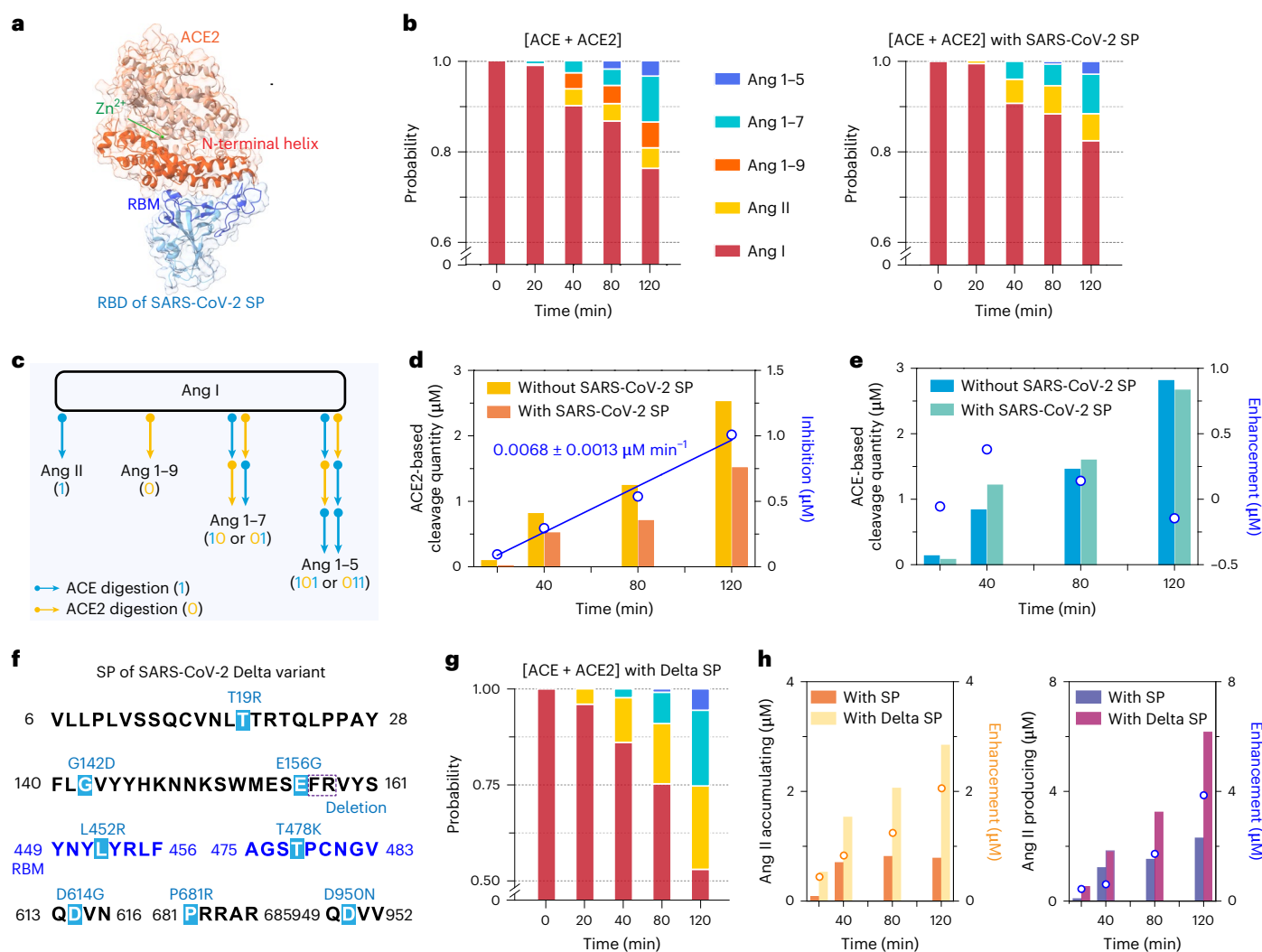
Fig. 4 | The effects of the SP of SARS-CoV-2 on the crosstalk between ACE and ACE2. a, Illustration of the binding between the SARS-CoV-2 SP and ACE2 (PDB 6M0J). **b**, Time-dependent probability of Ang peptides during the cleavage of Ang I by ACE2 and ACE without (left) and with (right) the SP of SARS-CoV-2, respectively. **c**, Illustration of Ang I metabolism pathways regulated by ACE and ACE2. **d**,**e**, Time-dependent cleavage quantity of ACE2 (**d**) or ACE (**e**), and the corresponding inhibition or enhancement (open circles) induced by SARS-CoV-2 SP. **f**, Mutation sites in the SP of the SARS-CoV-2 Delta variant. **g**, Time-dependent probability of Ang peptides during the cleavage of Ang I by ACE2 and ACE with Delta SP. **h**, Enhancement of Ang II accumulated and produced by the Delta SP compared to SP. The data were acquired in 1.0 M KCl with 10 mM HEPES and 10 μM ZnCl₂ at pH 8.0 under an applied potential of +140 mV. The concentrations of ACE and ACE2 were 36 nM and 1.2 nM, respectively, with 17 nM SP of SARS-CoV-2 or SARS-CoV-2 Delta variant, and an initial Ang I substrate concentration of 13.1 μM. The reaction temperature was set to 21 ± 1 °C.

observed for the reaction without ACE or with increasing ACE2 concentration, suggesting a complex mechanism between them. Furthermore, the effect of the SP of the SARS-CoV-2 Delta variant was evaluated, and the change in the interactions between the Delta SP and ACE2 was found to clearly induce a greater relaxation of ACE from the inhibition of ACE2 for Ang I cleavage, leading to a high Ang II level. This result suggests that the nanopore framework might also be applied to test the potential effect and roughly screen the possible variants of concern for SARS-CoV-2 in vitro. As the two active domains of ACE possess distinct substrate specificity for Ang peptides[35–37], the crosstalk between ACE and ACE2, and the disturbance of this crosstalk effect by the SARS-CoV-2 SP, might be attributed to the binding and/or cleavage of one domain of ACE by ACE2; this could be systematically investigated and might further suggest a new rapid intervention for the disease induced by SARS-CoV-2. Considering that the quantitative analysis of substrates with only one unit difference in real time and the simultaneous monitoring of the evolution of multiple components are ongoing challenges for MS and

fluorescence labelling, respectively, this nanopore-based approach can satisfy the requirements for high-precision analysis in terms of identification and quantification at the same time. Given that the sensitivity and efficiency of the nanopore single-molecule interface can be precisely regulated, and the temporal resolution of the nanopore when studying a reaction can be improved by developing a smarter algorithm and/or nanopore sensor with higher capture efficiency, in principle, the nanopore framework could be adapted for application to all biological crosstalk effects and could even be used to develop single-molecule temporal omics and reveal unknown biological processes.

Online content

Any methods, additional references, Nature Portfolio reporting summaries, source data, extended data, supplementary information, acknowledgements, peer review information; details of author contributions and competing interests; and statements of data and code availability are available at https://doi.org/10.1038/s41557-023-01139-8.

References

1. Ocaranza, M. P. et al. Counter-regulatory renin–angiotensin system in cardiovascular disease. *Nat. Rev. Cardiol.* **17**, 116–129 (2019).

2. Calvillo, L., Gironacci, M. M., Crotti, L., Meroni, P. L. & Parati, G. Neuroimmune crosstalk in the pathophysiology of hypertension. *Nat. Rev. Cardiol.* **16**, 476–490 (2019).

3. Fernández-Ruiz, I. ACE2 level as a marker of CVD. *Nat. Rev. Cardiol.* **17**, 759 (2020).

4. Cooper-DeHoff, R. M. & Johnson, J. A. Hypertension pharmacogenomics: in search of personalized treatment approaches. *Nat. Rev. Nephrol.* **12**, 110–122 (2016).

5. Oparil, S. et al. Hypertension. *Nat. Rev. Dis. Primers* **4**, 18014 (2018).

6. Santos, R. A. S. et al. The ACE2/angiotensin-(1–7)/MAS axis of the renin-angiotensin system: focus on angiotensin-(1–7). *Physiol. Rev.* **98**, 505–553 (2018).

7. Patel, V. B., Zhong, J.-C., Grant, M. B. & Oudit, G. Y. Role of the ACE2/angiotensin 1–7 axis of the renin-angiotensin system in heart failure. *Circ. Res.* **118**, 1313–1326 (2016).

8. Rice, G. I., Thomas, D. A., Grant, P. J., Turner, A. J. & Hooper, N. M. Evaluation of angiotensin-converting enzyme (ACE), its homologue ACE2 and neprilysin in angiotensin peptide metabolism. *Biochem. J.* **383**, 45–51 (2004).

9. Lan, J. et al. Structure of the SARS-CoV-2 spike receptor-binding domain bound to the ACE2 receptor. *Nature* **581**, 215–220 (2020).

10. Yan, R. et al. Structural basis for the recognition of SARS-CoV-2 by full-length human ACE2. *Science* **367**, 1444–1448 (2020).

11. Gheblawi, M. et al. Angiotensin converting enzyme 2: SARS-CoV-2 receptor and regulator of the renin-angiotensin system. *Circ. Res.* **126**, 1456–1474 (2020).

12. Tsuriel, S., Gudes, S., Draft, R. W., Binshtok, A. M. & Lichtman, J. W. Multispectral labeling technique to map many neighboring axonal projections in the same tissue. *Nat. Methods* **12**, 547–552 (2015).

13. Abdeladim, L. et al. Multicolor multiscale brain imaging with chromatic multiphoton serial microscopy. *Nat. Commun.* **10**, 1662 (2019).

14. Bosscher, K. D., Desmet, S. J., Clarisse, D., Estébanez-Perpiña, E. & Brunsveld, L. Nuclear receptor crosstalk—defining the mechanisms for therapeutic innovation. *Nat. Rev. Endocrinol.* **16**, 363–377 (2020).

15. Xu, H. et al. Protease-responsive mass barcoded nanotranslators for simultaneously quantifying the intracellular activity of cascaded caspases in apoptosis pathways. *Chem. Sci.* **11**, 5280–5288 (2020).

16. Branton, D. et al. The potential and challenges of nanopore sequencing. *Nat. Biotechnol.* **26**, 1146–1153 (2008).

17. Chavis, A. E. et al. Single molecule nanopore spectrometry for peptide detection. *ACS Sens.* **2**, 1319–1328 (2017).

18. Ouldali, H. et al. Electrical recognition of the twenty proteinogenic amino acids using an aerolysin nanopore. *Nat. Biotechnol.* **38**, 176–181 (2020).

19. Vergalli, J. et al. Porins and small-molecule translocation across the outer membrane of Gram-negative bacteria. *Nat. Rev. Microbiol.* **18**, 164–176 (2020).

20. Ying, Y.-L. & Long, Y.-T. Nanopore-based single-biomolecule interfaces: from information to knowledge. *J. Am. Chem. Soc.* **141**, 15720–15729 (2019).

21. Xue, L. et al. Solid-state nanopore sensors. *Nat. Rev. Mater.* **5**, 931–951 (2020).

22. Galenkamp, N. S., Biesemans, A. & Maglia, G. Directional conformer exchange in dihydrofolate reductase revealed by single-molecule nanopore recordings. *Nat. Chem.* **12**, 481–488 (2020).

23. Shi, W., Friedman, A. K. & Baker, L. A. Nanopore sensing. *Anal. Chem.* **89**, 157–188 (2016).

24. Li, M.-Y., Wang, Y.-Q., Ying, Y.-L. & Long, Y.-T. Revealing the transient conformations of a single flavin adenine dinucleotide using an aerolysin nanopore. *Chem. Sci.* **10**, 10400–10404 (2019).

25. Varongchayakul, N., Song, J., Meller, A. & Grinstaff, M. W. Single-molecule protein sensing in a nanopore: a tutorial. *Chem. Soc. Rev.* **47**, 8512–8524 (2018).

26. Cao, C. et al. Discrimination of oligonucleotides of different lengths with a wild-type aerolysin nanopore. *Nat. Nanotechnol.* **11**, 713–718 (2016).

27. Piguet, F. et al. Identification of single amino acid differences in uniformly charged homopolymeric peptides with aerolysin nanopore. *Nat. Commun.* **9**, 966 (2018).

28. Wang, Y., Gu, L.-Q. & Tian, K. The aerolysin nanopore: from peptidomic to genomic applications. *Nanoscale* **10**, 13857–13866 (2018).

29. Cressiot, B. et al. Aerolysin, a powerful protein sensor for fundamental studies and development of upcoming applications. *ACS Sens.* **4**, 530–548 (2019).

30. Huang, G., Voet, A. & Maglia, G. FraC nanopores with adjustable diameter identify the mass of opposite-charge peptides with 44 dalton resolution. *Nat. Commun.* **10**, 835 (2019).

31. Lucas, F. L. R. et al. The manipulation of the internal hydrophobicity of FraC nanopores augments peptide capture and recognition. *ACS Nano* **15**, 9600–9613 (2021).

32. Vickers, C. et al. Hydrolysis of biological peptides by human angiotensin-converting enzyme-related carboxypeptidase (ACE2). *J. Biol. Chem.* **277**, 14838–14843 (2002).

33. Buenning, P., Holmquist, B. & Riordan, J. F. Substrate specificity and kinetic characteristics of angiotensin converting enzyme. *Biochemistry* **22**, 103–110 (1983).

34. Ehlers, M. R. W. & Kirsch, R. E. Catalysis of angiotensin I hydrolysis by human angiotensin-converting enzyme: effect of chloride and pH. *Biochemistry* **27**, 5538–5544 (1988).

35. Guang, C., Phillips, R. D., Jiang, B. & Milani, F. Three key proteases—angiotensin-I-converting enzyme (ACE), ACE2 and renin—within and beyond the renin-angiotensin system. *Arch. Cardiovasc. Dis.* **105**, 373–385 (2012).

36. Deddish, P. A. et al. N-domain-specific substrate and C-domain inhibitors of angiotensin-converting enzyme. *Hypertension* **31**, 912–917 (1998).

37. Jaspard, E., Wei, L. & Alhenc-Gelas, F. Differences in the properties and enzymatic specificities of the two active sites of angiotensin I-converting enzyme (kininase II). Studies with bradykinin and other natural peptides. *J. Biol. Chem.* **268**, 9496–9503 (1993).

38. Lu, J. & Sun, P. D. High affinity binding of SARS-CoV-2 spike protein enhances ACE2 carboxypeptidase activity. *J. Biol. Chem.* **295**, 18579–18588 (2020).

39. Ogunlade, B. O., Lazartigues, E. & Filipeanu, C. M. Angiotensin Type 1 receptor-dependent internalization of SARS-CoV-2 by angiotensin-converting enzyme 2. *Hypertension* **77**, e42–e43 (2021).

40. Kutz, A. et al. Renin-angiotensin-aldosterone system peptide profiles in patients with COVID-19. *Eur. J. Endocrinol.* **184**, 543–552 (2021).

41. Ogunlade, B. et al. The actin bundling protein fascin-1 as an ACE2-accessory protein. *Cell. Mol. Neurobiol.* **42**, 255–263 (2022).

42. Kuba, K. et al. A crucial role of angiotensin converting enzyme 2 (ACE2) in SARS coronavirus-induced lung injury. *Nat. Med.* **11**, 875–879 (2005).

43. Lei, Y. et al. SARS-CoV-2 spike protein impairs endothelial function via downregulation of ACE 2. *Circ. Res.* **128**, 1323–1326 (2021).

Methods

Mutation, expression and purification of proaerolysin

The construction of recombinant proaerolysin plasmids is described in our previous work[44,45]. The mutant expression vectors were constructed by site-directed mutagenesis with high-fidelity polymerase chain reaction (PCR) enzymes (Invitrogen, 12368010). The following primers were used for plasmid mutation: K238Q, 5′-GAGCGAGCAAGTCACCACCAAAAACAAATTC-3′ (forward) and 5′-GGTGGTGACTTGCTCGCTCAGACCGTAGG-3′ (reverse); N226Q, 5′-CCGCAACCCAATGGAGCAAAACCAATACC-3′ (forward) and 5′-TTGCTCCATTGGGTTGCGGTATCGTAACG-3′ (reverse); T232K, 5′-AAACCAATAAATACGGTCTGAGCGAGAAAG-3′ (forward) and 5′-AGACCGTATTTATTGGTTTTGCTCCAG-3′ (reverse). The PCR cycling conditions and the expression and purification processes of proaerolysin roughly correspond to our previous studies. It should be noted that the expression temperature of the T232K mutation was shifted to 15 °C after the addition of IPTG with a final concentration of 0.4 mM to reduce the possible aggregation of misfolded proaerolysin.

Nanopore experiments

The nanopore experiment was performed on a Delrin bilayer cup (Warner Instruments), which was separated into *cis* and *trans* compartments by a 50-μm orifice. Note that the *cis* chamber was grounded. Both compartments were loaded with 1.0 ml of electrolyte solution, and a pair of Ag/AgCl electrodes connected to an Axopatch 200B amplifier (Molecular Devices) were immersed to apply potential. By using 30 mg ml⁻¹ 1,2-diphytanoyl-*sn*-glycero-3-phosphocholine (Avanti Polar Lipids, 850356) in decane (Sigma-Aldrich, 30540), a lipid bilayer was formed on the orifice. By injecting pre-activated aerolysin mutant protein adjacent to the orifice on the *cis* side, this could self-assemble to form a nanometre pore in the lipid bilayer. To prevent the possible cleavage of Ang peptides by trypsin, activation of the purified proaerolysin used in this work was carried out using Trypsin-agarose (Sigma-Aldrich, T1763) rather than trypsin-EDTA. After incubation with 0.03 U (~2.0 μl) trypsin-agarose for 1.0 ml of proaerolysin solution (1.0 mg ml⁻¹) for 6 h at 20 °C, the suspension was centrifuged at 12,000*g* for 10 min to pellet the trypsin-agarose. The current traces were amplified and measured with the Axopatch 200B amplifier equipped with a Digidata 1440A analog-to-digital converter (Molecular Devices). The current was filtered at 5 kHz and acquired at a sampling rate of 100 kHz with Clampex 10.4 software (Molecular Devices). The enzymes ACE and ACE2 were purchased from Sigma-Aldrich, the SPs of SARS-CoV-2, including WT and Delta variant, were purchased from Sino Biological. All Ang peptides were purchased from GL Biochem (purity >98%), and were not purified before the experiments. Of note, the purity of all the peptides used in the experiments was rechecked using HPLC (Supplementary Fig. 43).

Ang peptides identification and quantification. After a single stable and low-background aerolysin mutant nanopore was formed, the *I*–*V* curve of the mutant aerolysin was characterized to roughly determine the reliability of the pore. The analyte was then added to the *cis* chamber, and the single-channel events were measured with an applied potential. To determine the sensing capability of mutant aerolysins, each type of aerolysin was tested with three individual measurements with the applied voltage ranging from +80 mV to +160 mV. To identify the Ang peptides with T232K mutant aerolysin, the Ang peptides were added to the *cis* chamber one by one, carrying out at least 1.0 h of current recording to ensure full diffusion after adding each peptide. To establish the correlation between capture rates and Ang peptide concentrations, the Ang peptide was premixed with the detection solution to avoid diffusion-induced capture differences, and the capture rate for each concentration was taken from at least three individual measurements. Note that the storage concentrations of the Ang peptides were confirmed by ultra-violet (UV) analysis (Supplementary Fig. 44 and

Supplementary Table 3) using a NanoDrop 2000C spectrophotometer (Thermo Scientific).

Enzymatic catalysis processes monitoring. To avoid the uneven diffusion-induced capture rate change, the substrate Ang I was premixed with the solution in the *cis* chamber. After ensuring the reliability and stability of the constructed T232K mutant aerolysin nanopore as described in the previous section, the enzymes were added to the *cis* chamber. More importantly, to avoid possible diffusion from the *cis* to the *trans* chamber during reforming of the lipid membrane, which would result in a change in concentration of the substrate, enzyme and products, the same enzymatic reaction, including substrate and enzymes, was performed in the *trans* chamber.

Mass spectroscopy analysis

The enzymatic reactions were performed in the same conditions as used for the reactions in the nanopore approach, including the reaction volume (1,000 μl), pH (8.0), salt type and concentration (1.0 M or 0.15 M KCl), substrate quantity (4.0 μM or 13.1 μM Ang I), ACE and/or ACE2 concentration (ACE, 36 nM; ACE2, 23 nM or 1.2 nM), and temperature (21 ± 1 °C). At each time point, 200 μl of reaction solution was separated from the reaction mixture and quenched by incubating at 90 °C for 10 min in the metal bath. The reaction mixture was then loaded onto a C18 Ziptip set-up (Millipore) that had been washed with 100% acetonitrile and equilibrated with 0.1% trifluoroacetic acid (TFA). The Ziptip was washed with 0.1% TFA and the sample eluted in 75% acetonitrile containing 0.1% TFA. The desalted samples were identified and quantified using an Orbitrap Q Exactive high-resolution mass spectrometer (Thermo Scientific) equipped with a heated electrospray ionization source. The following generic MS tune parameters were used: spray voltage, 3.5 kV (positive mode); capillary temperature, 320 °C, sheath gas (nitrogen) flow, 35 arbitrary units (a.u.); auxiliary gas (nitrogen) flow, 10 a.u.; probe heater temperature, 400 °C. A full MS scan was acquired for each run in the range of m/z 200–2,000 with a resolving power of 140,000 full-width at half-maximum. The automatic gain control target value and maximum injection time used for the full MS scan were 3×10^6 and 50 ms, respectively. The raw data obtained from ESI-Quadrupole-Orbitrap MS were processed using Thermo Xcalibur software version 4.1.

HPLC analysis

HPLC analysis was performed on a Shimadzu LC-20AB HPLC system using an ACE C18-300 250 × 4.6 mm (5.0 μm) column and monitored with a UV (220 nm) detector. After injecting the peptide solution, the column was eluted with a linear gradient (~1–88%) of acetonitrile containing 0.1% formic acid from ~2 to 30 min at a flow rate of 1.0 ml min⁻¹.

Molecular dynamics simulation

Model construction. The wild-type aerolysin structure coordinates were obtained from the Protein Data Bank (PDB 5JZT)[46]. The aerolysin was first solvated by the SOLVATE program[47] to produces a 3-Å-thick shell of water around the aerolysin using eight Gaussians to approximate the protein surface, which was merged with a 200 Å × 200 Å path of 1,2-dimyristoyl-*sn*-glycero-3-phosphocholine (DMPC) lipid bilayer, aligned to the x–y plane with the hydrophobic β-barrel of aerolysin embedded in the bilayer and its hydrophilic cap protruding above the membrane. All the lipid and water molecules overlapping with the protein nanopore were removed. The nanopore–lipid system was solvated with pre-equilibrated TIP3P water molecules[48] using Visual Molecular Dynamics (VMD)[49]. K⁺ and Cl⁻ ions were added to the solution to neutralize the aerolysin system to a concentration of 1.0 M. The T232K and N226Q mutant aerolysins were constructed by mutating the amino-acid residues from WT aerolysin using the Mutator plugin in VMD[50].

System equilibrium and simulation. All MD simulation were performed using the program NAMD[51], with visualization and analysis

by VMD[49]. The aerolysin protein and oligonucleotide molecule were described by the CHARMM36 force field. After a 5,000-step minimization, the aerolysin nanopore system was equilibrated in the constant-temperature, constant-pressure (NPT) ensemble at 295 K and 1 atm for 2 ns, with the heavy atoms (non-hydrogen) of the protein restrained, and allowing relaxation of the lipid, water, ions and protein hydration atoms. Afterwards, the alpha carbons of the protein were still restrained, and the equilibration simulation lasted 20 ns. Next, all the restraints were removed, and the system was relaxed for 60 ns. All NPT ensemble simulations were carried out with a Langevin piston for pressure control and Langevin dynamics for temperature control[52]. Periodic boundary conditions were employed in all directions. The van der Waals energies were calculated using a 12-Å cutoff, and the particle-mesh-Ewald (PME) method was used to treat long-range electrostatics[53]. Additional 80-ns simulations with an electric field applied to each system (WT, N226Q, T232K and K238Q) were performed as an constant-temperature, constant-volume (NVT) ensemble without any positional restraint applied to the aerolysin side chain to simulate the application of a voltage bias of +120 mV. The electrostatic potential map of each system was then computed based on the last 10-ns simulation trajectory using the PME electrostatics plugin of VMD in accordance with previous work[54].

Data analysis

After current recording, the data were analysed using Mosaic 1.3 software[55], which fit the equations obtained in an equivalent circuit model of the nanopore system to each event. The scatter plots of peptide events could be divided into two parts, translocation events and collision events, according to our previous work[26]. For further analysis, including frequency calculation, capture efficiency normalization and events classification, the collision events that were normally shorter than ~0.2 ms were excluded. The blockade current was analysed statistically by using Gaussian fittings to event amplitude histograms. The duration time and inter-event time of characteristic events falling in the Gaussian peak were further analysed by fitting the histograms with a single exponential curve.

Capture rate calculation. Traditionally, the capture rate of a peptide is calculated from $f = 1/\tau_{on}$, where τ_{on} is the inter-event interval, with the histogram fitted into single exponential decline. It should be noted that this fitting process requires many inter-event intervals (normally >500) to ensure the accuracy of the fitted τ_{on} value, which leads to a requirement for a long recording time. We improved the calculation method for the capture rate by directly using the total event number $n_{peptide}$ during effective time $\tau_{effective}$. As illustrated in Supplementary Fig. 12, because the effective time for a certain peptide represents the time during which the peptide does not stay inside the pore, $\tau_{effective}$ can be calculated from $\tau_{effective} = \tau_{total} - \sum_{off\ peptide} \tau$. As shown in Supplementary Fig. 13, taking Ang II as an example, the $n_{peptide}$ of Ang II is proportional to $\tau_{effective}$, giving a stable $n_{peptide}/\tau_{effective}$ value. Also, the standard error of $n_{peptide}/\tau_{effective}$ from at least three independent measurements was lower than 4.4%, demonstrating the reliability of the improved calculation method. We compared the $n_{peptide}/\tau_{effective}$ and f calculated from the inter-event interval with a series of concentrations of Ang II ranging from 0.1 μM to 4.0 μM. The results showed that $n_{peptide}/\tau_{effective}$ was almost equal to f at each concentration of Ang II, and the standard curves for the concentration and capture rate ($n_{peptide}/\tau_{effective}$ or f) were also quite similar (Supplementary Figs. 13 and 14), with deviation lower than 5% (Supplementary Table 2), demonstrating the accuracy of the improved calculation method. Furthermore, to confirm the feasibility of this calculation method in estimating the concentration in the mixture, we calculated $n_{peptide}/\tau_{effective}$ for Ang II in the mixture in the presence of 0.50 M or 1.0 M of each of the Ang peptides (Ang I, Ang 1–9, Ang II, Ang 1–7 and Ang 1–5). The $n_{peptide}/\tau_{effective}$ values of Ang II are 2.91 ± 0.08 s⁻¹ and 6.95 ± 0.29 s⁻¹, giving estimated concentrations of

Ang II of 0.51 ± 0.07 μM and 1.1 ± 0.09 μM, respectively (by referring to the standard curves between the concentration and $n_{peptide}/\tau_{effective}$, as shown in Supplementary Fig. 13f), which are almost equal to the real concentrations of Ang II in the mixtures (0.50 μM and 1.0 μM). These results demonstrate the feasibility of using $n_{peptide}/\tau_{effective}$ for calculating the concentration of the peptides in the mixture. Therefore, in this Article, we calculated the $n_{peptide}/\tau_{effective}$ of each Ang peptide every 1 min to obtain the capture rate ratio, which could then be used to estimate their concentrations at every 1 min by combining with the capture efficiency of the Ang peptides.

Capture efficiency normalization. Due to the different lengths and net charges of the Ang peptides, the T232K mutant aerolysin has a distinct capture efficiency for the different Ang peptides. To quantify this capture efficiency among the Ang peptides, we introduced the capture efficiency ratio between the peptides. Because the differences in the frequency of events between Ang peptides with the same concentration represent their capture efficiency (P) difference, the capture efficiency ratio can be calculated from the frequency (f) of the events of each Ang peptide and their concentrations (c), as follows:

$$P_{Ang\,I} : P_{Ang\,1-9} : P_{Ang\,II} : P_{Ang\,1-7} : P_{Ang\,1-5}$$

$$= \frac{f_{Ang\,I}}{c_{Ang\,I}} : \frac{f_{Ang\,1-9}}{c_{Ang\,1-9}} : \frac{f_{Ang\,II}}{c_{Ang\,II}} : \frac{f_{Ang\,1-7}}{c_{Ang\,1-7}} : \frac{f_{Ang\,1-5}}{c_{Ang\,1-5}}$$

If the concentration of each peptide is same in the mixture when performing the experiments, the capture efficiency ratio can be directly estimated from the event frequency. To evaluate the capture efficiency ratio and its consistency in different concentrations, Ang I, Ang 1–9, Ang II, Ang 1–7 and Ang 1–5 were premixed in the solution with final concentrations of 0.50, 1.0 and 2.0 μM for each. The events were assigned to five Ang peptides based on the current blockage, current s.d. and duration, and $n_{peptide}/\tau_{effective}$ for the five peptides was analysed individually. The capture ratios for the five peptides were then calculated at the three different concentrations to verify the stability of the capture efficiency.

Ang peptides quantification. During the enzymic catalysis processes, given that the single amino acid and dipeptide cannot induce any current blockage on T232K mutant aerolysin (data not shown), the total concentration of detectable Ang peptides (Ang I, Ang 1–9, Ang II, Ang 1–7 and Ang 1–5) is equal to the initial concentration of substrate Ang I ($c_{0(Ang\,I)}$) at every time:

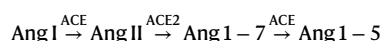$$c_{Ang\,I} + c_{Ang\,1-9} + c_{Ang\,II} + c_{Ang\,1-7} + c_{Ang\,1-5} = c_{0(Ang\,I)}$$

Because the capture efficiency ratios for the Ang peptides were quite stable at different concentrations, as already demonstrated (Supplementary Fig. 11), the concentration ratio of the Ang peptides can be estimated based on the capture rate ratio of each Ang peptide and their capture efficiency ratio. Note that the capture rate ratio of Ang peptides here was calculated from $n_{peptide}/\tau_{effective}$ of each peptide, as described above. In the mixture with total concentration ranging from 0.1 μM to 10.0 μM, the Ang peptides enter into the T232K mutant aerolysin as a non-competitive model, and the entering of each Ang peptide is hardly affected by the other peptides. Therefore, the $\tau_{effective}$ for each Ang peptide was calculated from the total duration of each Ang peptide. For example, for the capture rate of Ang I in each minute, $f = n_{Ang\,I}/(\tau_{1\,min} - \tau_{duration(Ang\,I)})$.

Kinetic constants calculation. According to the substrate/product concentration–reaction time curve, the rate of the reaction was calculated from the slope at a certain time point. It should be noted that there is an assumption in the Michaelis–Menten equation that the enzyme–substrate complex is in equilibrium with free enzyme and free substrate. Using the concentrations of enzymes used in Fig. 2 for kinetic constant calculations (0.036 μM for ACE and 0.023 μM for ACE2), after
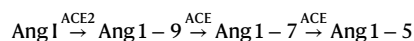
the rate of the reaction reaches a maximum, rates of reaction with the substrate ranging from ~3.2 μM to ~0.50 μM were used for calculation of the kinetic constant. The substrate-concentration-dependent reaction rate was then fitted to the Lineweaver–Burk equation to evaluate the kinetic constants of the enzymes.

SP inhibition efficiency calculation. The enzyme crosstalk effects of ACE and ACE2 contain the following potential catalysis pathways:

Pathway (a)

$$\text{Ang I} \xrightarrow{\text{ACE}} \text{Ang II} \xrightarrow{\text{ACE2}} \text{Ang } 1-7 \xrightarrow{\text{ACE}} \text{Ang } 1-5$$

Pathway (b)

$$\text{Ang I} \xrightarrow{\text{ACE2}} \text{Ang } 1-9 \xrightarrow{\text{ACE}} \text{Ang } 1-7 \xrightarrow{\text{ACE}} \text{Ang } 1-5$$

For both pathways, the formation of Ang 1–9, Ang 1–7 and Ang 1–5 must have been cleaved by ACE2 once. Therefore, the total cleavage quantity by ACE2 can be estimated from the concentrations of Ang 1–9, Ang 1–7 and Ang 1–5. Here we use the time-dependent concentration of ACE2-related products without and with SP of SARS-CoV-2 to calculate the average SP inhibition efficiency by linear fitting, as shown in Fig. 4d.

Data availability

Data supporting the findings of this study are available in the main text and the Supplementary Information. Additional raw data are available at https://doi.org/10.6084/m9.figshare.21621663. Source data are provided with this paper.

References

44. Wang, Y.-Q. et al. Rationally designed sensing selectivity and sensitivity of an aerolysin nanopore via site-directed mutagenesis. *ACS Sens.* **3**, 779–783 (2018).
45. Wu, X.-Y. et al. Precise construction and tuning of an aerolysin single-biomolecule interface for single-molecule sensing. *CCS Chem.* **1**, 304–312 (2019).
46. Iacovache, I. et al. Cryo-EM structure of aerolysin variants reveals a novel protein fold and the pore-formation process. *Nat. Commun.* **7**, 12062 (2016).
47. Grubmüller, H. & Groll, V. Solvate 1.0.1. http://www.mpibpc.mpg.de/grubmueller/solvate (1996–2010).
48. Jorgensen, W., Chandrasekhar, J., Madura, J., Impey, R. & Klein, M. Comparison of simple potential functions for simulating liquid water. *J. Chem. Phys.* **79**, 926–935 (1983).
49. Humphrey, W., Dalke, A. & Schulten, K. VMD: visual molecular dynamics. *J. Mol. Graph.* **14**, 33–38 (1996).
50. MacKerell, A. D. Jr et al. All-atom empirical potential for molecular modeling and dynamics studies of proteins. *J. Phys. Chem. B* **102**, 3586–3616 (1998).
51. Phillips, J. et al. Scalable molecular dynamics with NAMD. *J. Comput. Chem.* **26**, 1781–1802 (2005).
52. Feller, S., Zhang, Y., Pastor, R. & Brooks, B. Constant pressure molecular dynamics simulation: the Langevin piston method. *J. Chem. Phys.* **103**, 4613–4621 (1995).
53. Batcho, P., Case, D. & Schlick, T. Optimized particle-mesh Ewald/multiple-time step integration for molecular dynamics simulations. *J. Chem. Phys.* **115**, 4003–4018 (2001).
54. Aksimentiev, A. & Schulten, K. Imaging α-hemolysin with molecular dynamics: ionic conductance, osmotic permeability and the electrostatic potential map. *Biophys. J.* **88**, 3745–3761 (2005).
55. Balijepalli, A. et al. Quantifying short-lived events in multistate ionic current measurements. *ACS Nano* **8**, 1547–1553 (2014).

Acknowledgements

Author contributions

J.J., M.-Y.L. and Y.-T.L. conceived the project. Y.-T.L. supervised the project. J.J. carried out experiments and performed data analysis with assistance from M.-Y.L. M.-Y.L. performed molecular dynamics simulations. X.-Y.W. and M.-Y.L. produced the mutant proaerolysin. J.J., M.-Y.L., Y.-L.Y. and H.-X.H. drew the figures. M.-Y.L. and J.J. prepared the manuscript. All authors critically reviewed the manuscript.

Competing interests

The authors declare no competing interests.

Additional information

Supplementary information The online version contains supplementary material available at https://doi.org/10.1038/s41557-023-01139-8.

Correspondence and requests for materials should be addressed to Yi-Tao Long.

Peer review information *Nature Chemistry* thanks Catalin Filipeanu and the other, anonymous, reviewer(s) for their contribution to the peer review of this work.

Reprints and permissions information is available at www.nature.com/reprints.